

1 Assessment of the predictive capabilities of discrete element models for
2 flexible rockfall barriers

3 Loïc Dugelas^{a,*}, Jibril B. Coulibaly^b, Franck Bourrier^c, Stéphane Lambert^c, Marie-Aurélie
4 Chanut^b, Ignacio Olmedo^d, François Nicot^c

5 ^aUniv. Grenoble Alpes, Irstea, LESSEM, 38000 Grenoble, France

6 ^bGeological Hazards Team, Cerema Centre-Est, 25 Avenue François Mitterrand, CS 92803, 69674 Bron Cedex,
7 France

8 ^cUniv. Grenoble Alpes, Irstea, ETNA, 38000 Grenoble, France

9 ^dNGE Fondations, 6 rue de la Métallurgie, 38240 Domène, France

10 **Abstract**

This paper addresses the use of discrete element modeling approaches for predicting the impact response of flexible rockfall protection barriers. In this purpose, two different models are considered and their results are compared to detailed results from full-scale impact experiments. The studied barrier is a prototype made from a 4-contacts ring net and having a 270 kJ nominal capacity. The two discrete elements method models, developed by separate entities with different codes (Yade-DEM and GENEROCK), use different models for the ring net, the cables and cable-net connections, while other structural elements are modelled the same way : posts, anchors, energy dissipating devices, and boulder. The models for the structural elements (ring net, energy dissipating devices) are calibrated individually from quasi-static tensile tests results. The barrier model is then created assembling the structural elements, before being impacted. The tests consist in a impacting in its center a 3-module barrier, first, to one high kinetic energy impact and, second, to three consecutive impacts with a lower kinetic energy. The models results are confronted to measurements made during the experiments, considering a large set of parameters. Both models reveal satisfactory in predicting the structure response, on quantitative and qualitative points of view, and considering the boulder displacement, forces in the main cables and forces acting within the various energy dissipating devices. The quality of the prediction by each model compared to the other depends on the considered parameter. Little deviations from the experimental results are attributed to the model calibration procedure and to slight differences between the real structure and the modeled ones. In the end, the DEM approach appears suitable for modelling flexible barriers in complex loading conditions (high velocity and successive impacts).

11 **Keywords:** Rockfall flexible barrier, Experimental, Discrete Element Method, Ring net

*Corresponding author

Email address: loic.dugelas@irstea.fr (Loïc Dugelas)

12 Introduction

13 Rockfall is a critical issue in mountainous areas where mitigation measures must be used to
14 protect infrastructures and people from such hazards [Volkwein et al., 2011]. Among the numerous
15 existing protection systems, flexible rockfall barriers are efficient, lightweight and stand as practical
16 solutions to mitigate rockfalls. These barriers are highly deformable structures that can withstand
17 impacts and stop boulders propagating with kinetic energy ranging from 100 kJ up to 10,000 kJ
18 [Lambert and Nicot, 2011]. Determination of rockfall barriers performances has become crucial
19 over time because of their widespread use and the need to guarantee a given protection level.
20 Numerous experimental campaigns have been carried out over the past decades to evaluate the
21 impact energy, i.e. the kinetic energy of the boulder upon impact, one given technology can
22 withstand [McCauley et al., 1985, Smith and Duffy, 1990, Andrew et al., 1998, Muraishi et al.,
23 2005, Peila et al., 1998, Heiss, 2004, Gerber and Böll, 2006, Gottardi and Govoni, 2010, Bertrand
24 et al., 2012]. Insights from experimental campaigns have led to the development of standardized
25 testing methods and guidelines such as the European Assessment Document (EAD) for rockfall
26 protection systems [EOTA, 2018]. Well-instrumented full-scale tests can provide very informative
27 data but require extensive infrastructures and are very costly. In parallel, numerical modeling
28 techniques have been used to simulate impact tests and to obtain new insight into the barrier
29 behavior at a fraction of the full-scale testing costs. Seminal contributions [Nicot et al., 2001b,
30 Cazzani et al., 2002, Volkwein, 2005] introduced new modeling concepts and showed capabilities to
31 simulate the complex nonlinear dynamic response of rockfall barriers under impacts. These works
32 opened the way for the more recent developments taking advantage of increased computational
33 power to implement more complex models [Bertrand et al., 2012, Escallón et al., 2014, 2015,
34 Mentani et al., 2018, Yu et al., 2018], to perform parametric studies [Tran et al., 2013, Spadari
35 et al., 2012, Bourrier et al., 2015, Toe et al., 2018, Castanon-Jano et al., 2018, Coulibaly et al., 2019]
36 and to investigate failure mechanisms [Hambleton et al., 2013, Mentani et al., 2016]. Predictive
37 capabilities of numerical models allow a reduction in the number of full-scale tests to be performed.

38 The numerical tools used to analyze flexible rockfall barriers present unavoidable limitations,
39 mainly due to the complexity of the dynamic behavior of the structure upon impacts, and the
40 comprehensive assessment of their strengths and limits remains a difficult task. All the modeling

41 codes are readily not available for use, some of them are restrained by intellectual property, and
42 no benchmark or comparative studies between models is known to the authors. Early models have
43 focused on the overall response of the structure. Their coarse discretization and limited complexity
44 do not provide direct access to local information regarding the structure. Recent models have
45 been made increasingly complicated and sometimes unsuitable for current practical engineering
46 applications. To date, there is little quantification of the models capacities to reproduce a given
47 set of properties of a rockfall barrier response. Such quantification should include comparisons of
48 forces, boulder and structure kinematics over the entire loading duration for various loading cases.
49 In the same time, the computational cost of simulations must be kept within reasonable bounds
50 for risk management or industrial time scale of interest. Consequently, the capacities of the model
51 to capture the behavior of rockfall barriers while remaining computationally efficient have to be
52 quantified.

53 To quantify and compare the capacities of the models, a research group supported by the
54 French national project C2ROP (Rockfall hazards, Protective structures and Risk mitigation) has
55 carried out experimental and numerical research works on a prototype rockfall barrier. C2ROP is
56 an initiative clustering research laboratories, design offices, manufacturers and public authorities
57 around rockfall risk management in mountainous areas. Extensive experimental campaigns were
58 conducted to specify the responses of the components and of the entire barrier under different
59 loading conditions. A deep investigation of the structure response under single and consecutive
60 impacts was made to explore the complex and variable structure response with large deformations
61 and observed asymmetric diffusion of the forces. The experimental data gathered was used to
62 assess the predictive capacities of two models in this complex context. The models, developed
63 independently by contributors of the C2ROP project, are both based on a Discrete Element Method
64 (DEM) but present different modeling features and assumptions.

65 In the following sections, the prototype barrier is first introduced. Description of the barrier
66 geometry and technology and characterization tests of the barrier individual components as well as
67 full-scale impact tests procedures are detailed in section 1. The two DEM models of the barrier are
68 then detailed and the differences in modeling strategy and assumptions between the two approaches
69 are highlighted in section 2. A detailed description of the response of the barrier based on the

70 experimental full scale tests results is proposed in section 3. This is followed in section 4 by an
71 evaluation of the predictive capacity of both discrete element method models in comparison to the
72 experimental data. A discussion of the strengths, limitations and scope of use of these models is
73 also included in this section.

74 1. Rockfall barrier

75 The present section describes the investigated rockfall barrier, in terms of technology, dimen-
76 sions and position of the elements. The experiments done for the calibration and validation of the
77 structure models are also detailed.

78 1.1. General description

79 The prototype rockfall barrier was designed in collaboration between the manufacturers and
80 researchers of the C2ROP Project. The expected capacity of the barrier corresponds to a single
81 centered impact with maximum energy of 270 kJ (corresponding to a boulder with a mass of 740
82 kg, impacting at a normal velocity of 27 m/s). The barrier is installed on a vertical cliff with a 5°
83 horizontal inclination.

84 The three modules of the barrier (5 x 2.75 m) are installed between 4 posts, stabilized with 14
85 cables. A four-contacts ring net (one ring connected to 4 rings - Figure 1) is used. Each net module
86 (11 x 8 rings) is made up of 274 mm diameter rings (mass: 0.25 kg) with a section diameter of 7.5
87 mm.

88 The interception net is supported by 10 cables (12 mm diameter) weaved into the external
89 rings (Figure 2.a). The net supporting cables are connected to a post or an anchor by a friction
90 energy dissipating device (Figure 3). All in all, 18 energy dissipating devices connect the cables
91 supporting the net to a post or a lateral anchor. The friction energy dissipating devices work as
92 follow: once the tension in the cable reaches a threshold value, the cable slides in the device and
93 dissipates energy.

94 Additional upstream, downstream and lateral cables (16 mm diameter) connect the top of the
95 posts to the anchors (Figure 2.b). The posts are the only components subjected to compressive
96 loads. These consist of cylinders, 2.75 m in length and 43.6 kg in mass, with external and internal

97 diameters of 88.9 and 72.9 mm, respectively. The base of the posts is attached to the cliff with an
 98 articulated connection leaving the rotation around the longitudinal axis free.



Figure 1: 4-contacts ring net [Coulibaly et al., 2017b].

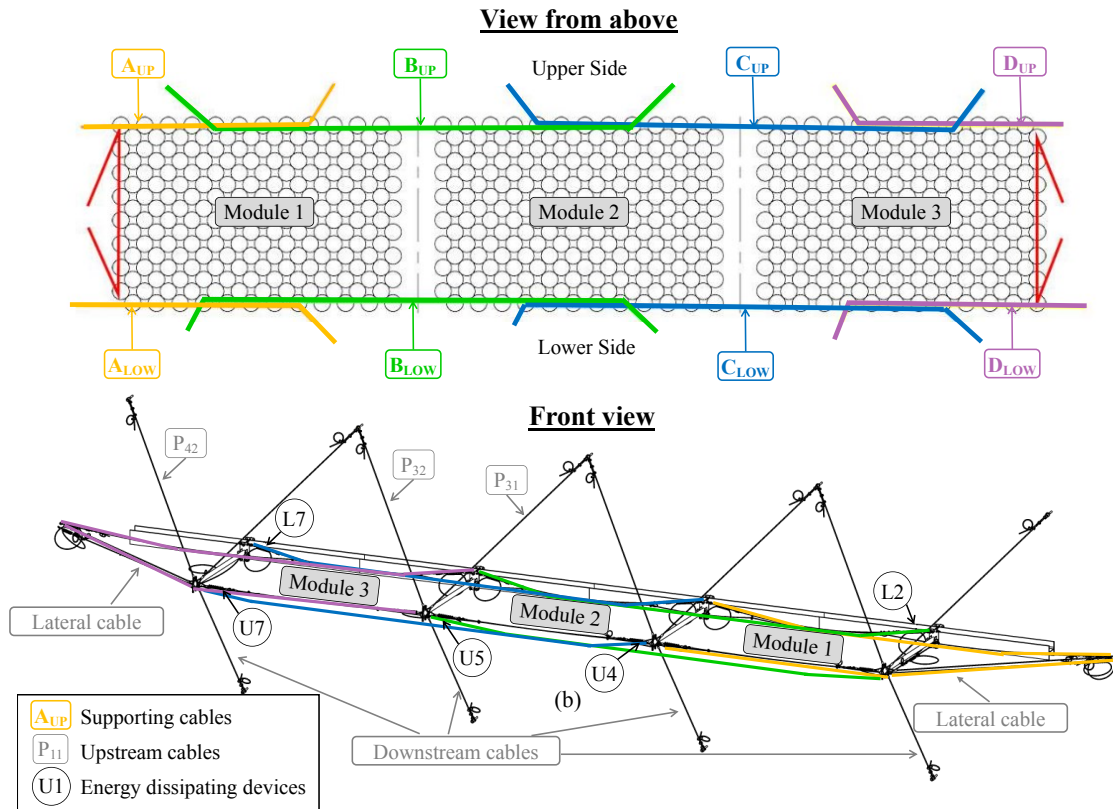


Figure 2: Cables and energy dissipating devices location and identification.

99 *1.2. Elements characterization*

100 For the models calibration (section 2.3), experiments were run to characterize the elements of
 101 the barrier. Static loading were chosen because of their set up simplicity, avoiding the launch of a
 102 boulder necessary in dynamic experiments. The interception structure and the energy dissipating



Figure 3: Friction energy dissipating device (GTS).

103 devices were tested into this study, the tests realized are introduced herein. The mechanical
104 specifications of the other elements were taken from literature.

105 *Interception structure*

106 Tensile tests on single rings and on 3 x 3 rings panels were carried out. At the scale of a single
107 ring, two-point (Figure 4.a) and four-point tensile tests (Figure 4.b) were conducted. For the 3 x
108 3 ring panels, a quasi-static displacement was applied to 3 rings on one side of the panel, while the
109 rings on the opposite side were maintained fixed (Figure 4.c). On the two other sides, translation
110 was possible along the loading direction only. During all these tests, the evolution of the forces
111 at the anchors was recorded against the displacements of these points. A detailed description of
112 these tests can be found in [Coulibaly et al. \[2017b\]](#).

113 *Energy dissipating devices*

114 Three quasi-static tests were conducted with the energy dissipating devices. The devices were
115 installed on a cable fixed at one extremity and subjected to a quasi-static displacement at the
116 other extremity. The force in the cable and the displacement at the moving extremity were both
117 recorded.

118 *1.3. Full scale impact tests*

119 Complete full-scale structures were subjected to both single and consecutive impacts experi-
120 ments. The impacting boulder was designed following the EAD recommendations [[EOTA, 2018](#)]:
121 a polyhedron with an external length of 0.75 m and a mass of 740 kg.

122 Two tests (SI_{Exp1} and SI_{Exp2}) were performed on two different structures with same charac-
123 teristics to study the structure response to single centered impacts with energy level at the limit
124 of the structure capacity (270 kJ, with an impact velocity of 27 m/s). The aim was to assess the
125 variability of the experimental results. Second, three consecutive impacts (CO_{Exp}^1 , CO_{Exp}^2 and
126 CO_{Exp}^3) on the same structure with reduced impact energy (90 kJ, with an impact velocity of 15.6
127 m/s) were carried out to analyze the structure response when plastic deformations are likely to
128 have developed.

129 The impacted structures were instrumented with force sensors (acquisition frequency: 10 kHz)
130 to record the evolution of the forces in three upstream cables (P_{31} , P_{32} and P_{42}), and three energy
131 dissipating devices on the supporting cables (L2, L7 and U7) (Figure 2). Two high speed cameras,
132 with a frame rate of 500 Hz, were used to capture the boulder vertical displacement (from the net-
133 boulder contact until the boulder stops) and the global deformation of the structure. A 3600 Hz
134 bandwidth accelerometer was set up in the impacting boulder. After each impact, the elongation
135 of the energy dissipating devices and the elongation of the net were measured. The former will be
136 introduced as the cable elongation, it corresponds to the sum of the maximum elongations of the
137 two energy dissipating devices connected to the studied cable (e.g. the elongation of cable C_{UP}
138 is the sum of the elongations of the devices U4 and U7). For all the measurements, the origin of
139 time ($t = 0$) corresponds to the instant of contact between the boulder and the net.

140 Section 3 introduces the results of these full scale tests. The forces recorded with the sensors are
141 explored, as well as the boulder vertical displacement and the elongation of the energy dissipating
142 devices. A deep analysis of the response of the structure under single and consecutive impacts are
143 respectively in section 3.1 and section 3.2.

144 2. DEM modeling of the barrier

145 Two models of the barrier presented in section 1 were developed separately. These models are
146 based on the same general principles with different assumptions and modeling strategies.

147 2.1. General principles

148 The structure introduced in section 1.1 was modeled using a Discrete Element Method (DEM).
149 This method has been widely used [Nicot et al., 2001a, Bertrand et al., 2008, Thoeni et al., 2013,

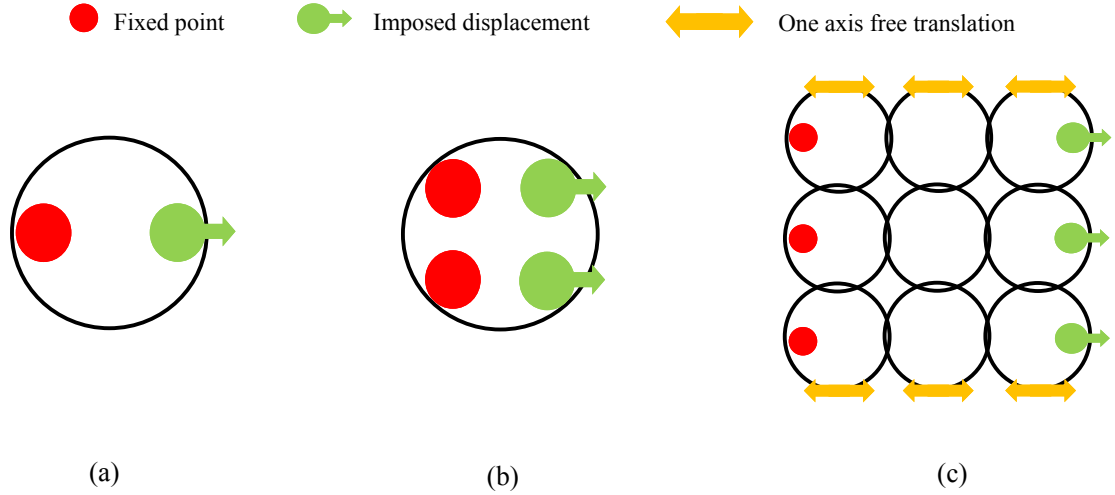


Figure 4: Representation of the tensile tests on the rings: 2 points test (a), 4 points test (b), 3 x 3 rings panel test (c).

150 Bourrier et al., 2015, Albaba et al., 2017, Coulibaly et al., 2019] to model rockfall protection barriers
 151 as it allows explicit and simple integration of large displacements and efficient implementation of
 152 multi-body contacts and dynamics. Instead of focusing, as classically in the literature, on a single
 153 model of a specific barrier, this study presents two models, developed separately, to analyze the
 154 response of the same barrier. The two models (model A and model B) have been developed using
 155 the codes Yade-DEM [Šmilauer et al., 2015] and GENEROCK [Coulibaly et al., 2019], respectively.
 156 Different assumptions were made, integrating different levels of complexity for the various structure
 157 components, besides few elements are modeled in the same way. The different modeling approaches
 158 considered are representative of existing ones in the literature. Consequently, the comparison of
 159 the models responses gives an overview of the consequences of the modeling choices.

160 For both models, each element (ring net, cables, energy dissipating devices, posts, connections)
 161 is first modeled individually (Section 2.2) and the element models are calibrated (Section 2.3)
 162 using data from the static experiments described in section 1.2 and from the literature. Second,
 163 the complete barrier is modeled by assembling the element models according to the geometry of
 164 the barrier with only rigid assembly between the elements. Finally, the relevance and accuracy of
 165 the models are assessed from the analysis of predictive simulations of the impact tests on the full
 166 structure described in section 1.3. This assessment is the purpose of section 4.

167 2.2. Element Models

168 *Retaining net*

169 Two different models of the ring net were used. A 6-contacts ring model developed by [Nicot et al.](#)
170 [\[2001a\]](#) (Figure 5.a) was adapted for 4-contacts ring nets and integrated into model A. In this model,
171 each ring is represented by a single spherical particle at its center, and remote interactions model the
172 contacts between neighbouring rings using piece-wise linear force-displacement relationships. These
173 relationships are characterized by three moduli associated with the loading phase and one modulus
174 associated with the unloading one. A more complex ring model [\[Coulibaly et al., 2017b\]](#) was used in
175 model B. This model is based on the location of 4 particles at the contact points between the rings,
176 except for the external ones (in contact with supporting cables) modeled with three particles. The
177 interactions between these particles are governed by three elasto-plastic constitutive relationships
178 for 2 inner linkages, 4 side linkages and one perimeter linkage (Figure 5.b). The full description
179 of this model is given in [Coulibaly et al. \[2017b\]](#) detailing the 8 parameters for the inner and side
180 linkages (respectively k_d, d_{ih}, a_d, b_d and k_s, s_{ih}, a_s, b_s), and the 6 parameters for the perimeter
181 linkage ($k_b, k_t, L_r, L_{ih}, a_p, b_p$).

182 *Cables*

183 In both models, the cables are modeled by series of articulated elements. These elements are
184 only subjected to tensile forces. Model A describes explicitly the cable as a set of spheres connected
185 by cylinders elements that have the same diameter as the cable. Model B uses material points
186 linked by remote interactions. In both cases, the mass of the cable is distributed to the supporting
187 elements (spheres or material points). 10 and 5 supporting elements per meter are used for model
188 A and model B, respectively.

189 *Cable-net connection*

190 The complex interlacing between the net and the supporting cables plays an important role in
191 the structure response. The so-called curtain effect resulting from this sliding has been shown to
192 have a significant influence on the structure response [\[Coulibaly et al., 2019\]](#). In the first model,
193 it is accounted for using sliding rings located at the attachment points of the net on the cables
194 (Figure 6), as per [Albaba et al. \[2017\]](#). The sliding rings, made up of four rigid cylinders, surround

195 the supporting cable and interact with it using an elasto-frictional contact model. In model B, a
196 frictional sliding model of the points of the cables connected to the net is implemented [Coulibaly
197 et al., 2018]. Model B describes this system as a collection of sliding and non-sliding nodes,
198 corresponding to the net and cable respectively. The complete presentation of this model is given
199 in Coulibaly et al. [2018].

200 *Posts*

201 The posts are modeled as cylindrical beams in model A (11 cylinder elements of 0.25 m length
202 for each post) whereas they are assumed to be rigid in model B.

203 *Energy dissipating devices*

204 The same model was used for the energy dissipating devices in both models. It consists in
205 two particles initially spaced by the length of the device and linked by a remote interaction. A 3
206 parameters (threshold force F_y , elastic modulus K_1 and plastic modulus K_2) elasto-plastic Prager
207 model is used to describe the mechanical behavior of the dissipating devices observed in quasi-static
208 experiments (section 1.2).

209 *Anchors and boulder*

210 The same modeling assumption was taken for anchors and boulder as well. The anchors are
211 modeled as fixed points and the impacting boulder is modeled as a rigid body, with a geometry
212 in accordance with the EAD recommendation [EOTA, 2018]. The boulder interacts with the net
213 using an elasto-frictional contact model.

214

215 The modeling assumptions associated with models A and B are summarized in Table 1.

216 *2.3. Models Calibration*

217 All the parameters of the element models introduced in section 2.2 are calibrated using data
218 from the experimental campaign described in section 1.2, or from literature data. This section
219 describes the calibration process for each component and refers to existing documents where more
220 details concerning the calibration can be found. The interception structure and energy dissipating
221 devices are calibrated using specific experimental data, while the other elements are calibrated
222 using literature data.

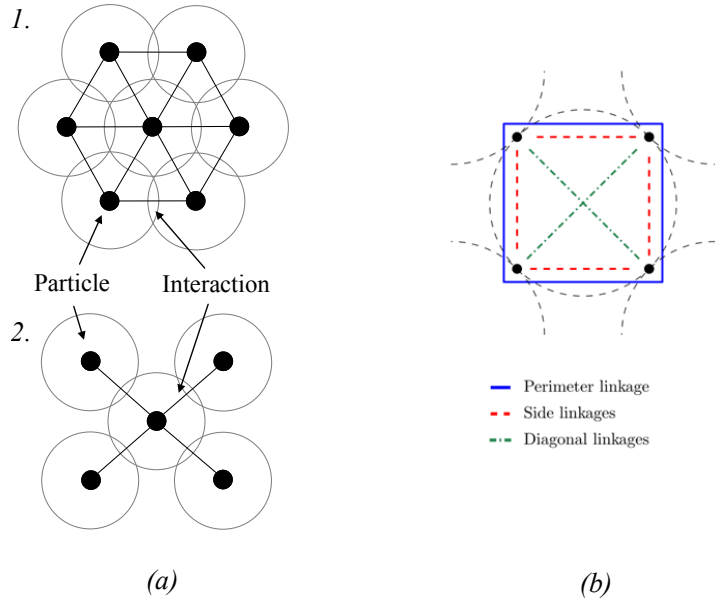


Figure 5: Nicot's 6-contacts ring net model [Nicot et al., 2001a] (a.1), 4-contacts ring net adapted model (a.2), Coulibaly's 4-nodes ring model [Coulibaly et al., 2017b].

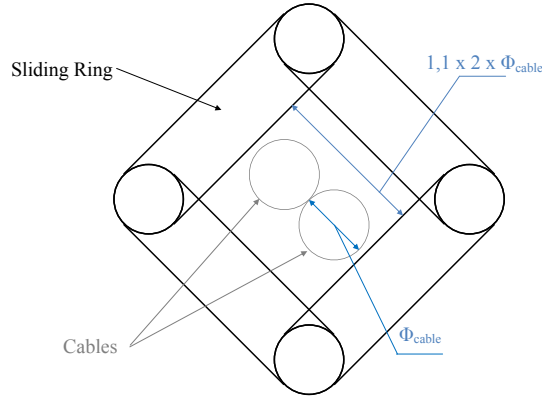


Figure 6: Sliding ring model from Albaba et al. [2017].

Component	model A	model B
Ring Net	Adaptation of Nicot's model [Nicot et al., 2001a]	Coulibaly's ring model [Coulibaly et al., 2017b]
Cables	Succession of articulated rigid plain cylinders 10 nodes per meters	Articulated rigid elements 5 nodes per meters
Energy dissipating devices	Two particles linked by remote interaction	
Posts	Succession of articulated rigid plain cylinders	Rigid rod
Anchors	Fixed points	
Cable-net link	Sliding rings model [Albaba et al., 2017]	Sliding nodes model [Coulibaly et al., 2018]
boulder	Polyhedron shape rigid body	

Table 1: Modeling assumptions for models A and B.

223 *Retaining net*

224 The net model integrated in model A is calibrated using the results of quasi-static tensile tests
225 on 3 x 3 rings panels (Section 1.2). The calibration allows to fit the experimental response using
226 a three-linear curve (Figure 7). The values of calibration parameters are specified in table 2. The
227 14 parameters of the ring net model used in model B were calibrated using 2 points and 4 points
228 quasi-static tensile tests. The complete detailed calibration process is available in Coulibaly et al.
229 [2017b] (Section “Model Calibration”) and the parameters values from Coulibaly [2017a] (Chapter
230 5, section 3) are presented in table 3.

231 *Energy dissipating devices*

232 The energy dissipating device model is similar in model A and B. It is calibrated from quasi-
233 static tests. Quasi-static tests are faster and easier to set up than dynamic ones, where the launch
234 of a boulder is needed. They also guarantee more reproducible loading conditions and, thus, exhibit
235 smaller variability. The values for the 3 parameters of the model are $F_y = 25$ kN, $K_1 = 250$ kN/m
236 and $K_2 = 7.143$ kN/m (Figure 8). It must be noted that the response of energy dissipating devices
237 to realistic dynamic loading conditions is expected to be slightly different from quasi-static ones
238 [Castanon-Jano et al., 2017].

239 *Other elements*

240 Finally, the parameters of the cables and posts models are calibrated using information obtained
241 from the literature and from the manufacturers [Feyrer, 2015] detailed in table 4. The cable-net
242 interaction, controlled by frictional processes, is characterized by a friction coefficient of 0.18, as
243 proposed by Albaba et al. [2017] for model A, whereas a friction coefficient of 0.3 is chosen for
244 model B [Coulibaly, 2017a].

Elongation range (m)	Modulus (kN/m)
0 - 0.058	44
0.058 - 0.082	256
0.082 - 0.1	1667
> 0.1	Failure

Table 2: Model A net interaction calibration parameters.

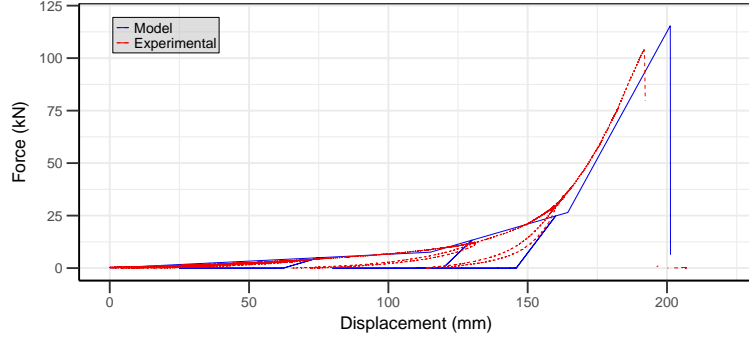


Figure 7: Force over displacement for tensile test on 3 x 3 rings: net model A results against experimental results.

Parameter	Value (3 nodes)	Value (4 nodes)
k_b (N/m)	15533	28106
k_t (N/m)	1450446	1684249
k_d (N/m)	70120	2893
k_s (N/m)	10787	10787
L_r (m)	0.8524	0.8475
L_{ih} (m)	0.700	0.7749
d_{ih} (m)	0.2531	0.314
s_{ih} (m)	0.1938	0.1938
a_p	1731	30479
a_d	0	4955179
a_s	0	0
b_p	3.163	3.588
b_d	0	5.198
b_s	0	0

Table 3: Model B net linkages calibration parameters [Coulibaly, 2017a].

Cable	Upstream	Downstream	Lateral	Supporting
Diameter (mm)	16	16	16	12
Linear mass (kg/m)	0.98	0.98	0.98	0.55
Failure force (kN) (from manufacturer)	168	168	168	94
Young Modulus (GPa)	100	100	100	100

Table 4: Cables properties.

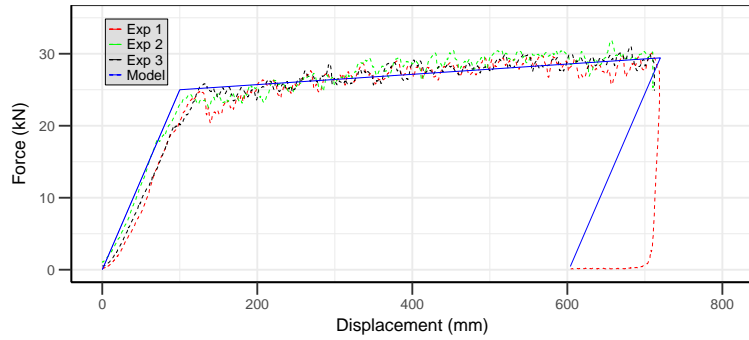


Figure 8: Force over energy dissipating device displacement along quasi-static tensile loading paths: Prager model results against experimental results.

245 *2.4. Simulation campaign*

246 Both a "single impact" simulation and a "consecutive impacts" simulation were performed. The
247 "single impact" simulation consists of one 270 kJ energy centered impact (740 kg boulder with an
248 impact velocity of 27 m/s). The "consecutive impacts" simulation consists of 3 consecutive impacts
249 at a 90 kJ energy level (740 kg boulder, 15.6 m/s), corresponding to one third of the energy level
250 of the "single impact" simulation.

251 The barrier models are created using the design introduced in section 1.1. On-site geometrical
252 adjustments during the installation of the full scale barrier and small variations in the impact point
253 location were not considered.

254 Before each impact simulation, the barrier model is left for 2 seconds under gravity loading. For
255 the single impact, the following phase consists of the impact, lasting 0.75 s. For the consecutive
256 impact simulations, a first impact is run during 0.4 sec. When the boulder reaches static equilib-
257 rium, it is removed. The barrier is then left under gravity, until it reaches a second equilibrium
258 state without boulder. The second and third impacts are simulated, following the same procedure
259 (Figure 9).

260 The same timestep, set at $\tau = 10^{-5}$ s, is used for all simulations and for both models. For
261 model A, the "consecutive impacts" simulation (gravity deposition and three impacts - Figure
262 9) requires 2175 seconds computation time using an Intel Core i7-6820HQ CPU 2.70 GHz CPU,
263 which corresponds to a temporal factor (simulation time/simulated time) of 102.5. For model B, it
264 requires 2671 seconds to simulate the consecutive impacts test using an Intel Core i3-4100M 2.50
265 GHz CPU, giving a temporal factor of 126. The comparison between the two models, in terms of
266 their ability in predicting the structure response, is thus not biased by any significant difference in
267 computation time efficiency.

268 For all impact tests, classical quantities used for assessment purposes according to the EAD
269 recommendations [EOTA, 2018] are monitored. The residual height of the barrier after impact,
270 defined as the horizontal distance between the supporting cables after impact. Also, the boulder
271 vertical displacement is recorded from the beginning of the impact (net-boulder contact) until it
272 stops.

273 Quantities of specific interest for the design of flexible barriers are also measured. The analysis

274 focuses on the evolution of the forces into three energy dissipating devices (L2, L7 and U7 - Figure
 275 2), on the evolution of the forces in three upstream cables (P_{31} , P_{32} and P_{42} - Figure 2), and on
 276 the maximum elongation of each energy dissipating devices.

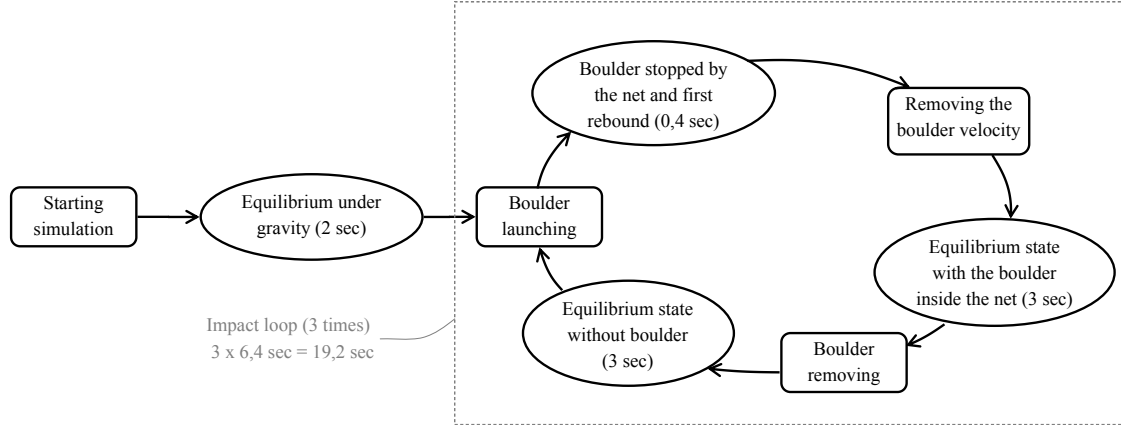


Figure 9: Simulation steps.

277 3. Structure response

278 The response of the structure is presented and discussed based on the real-time measurements
 279 of the boulder vertical displacement, cable elongation and forces acting on the energy dissipating
 280 devices and in the upstream cables. This analysis aims at highlighting trends and specific features
 281 of the spatial-temporal response of the structure during the single and the consecutive impacts
 282 tests.

283 3.1. Single impact test

284 The two single impact experiments (SI_{Exp1} and SI_{Exp2}) show qualitatively similar responses
 285 for the barrier in terms of rock block braking (Figure 10), exhibiting two distinct phases, from the
 286 very beginning of the boulder-structure contact ($t=0$).

287 During the first phase, defined as the pre-tensile phase ($t < 70$ ms, approximately), the boulder
 288 velocity exhibits negligible variation as shown by the linear evolution of the vertical displacement
 289 over time. No significant resisting force is applied to the boulder during this phase because the
 290 net is subjected to geometrical rearrangements (Figure 10). This phase is associated to a change
 291 in the net geometrical configuration until high tensile forces develop into the net. These forces
 292 are progressively transmitted towards the other structure components, in particular the energy

293 dissipating devices until their activation as observed in figure 11. In the same time, sliding of the
294 net on the supporting cables was observed with the high speed cameras.

295 The energy dissipating devices activation induces an increase in the length of the supporting
296 cables devices. This modifies the shape of the complete structure favouring a direct transfer of the
297 forces from the impact zone to the anchors, through the energy dissipating devices. This corre-
298 sponds to the second phase of the structure response (namely the reaction phase) with significant
299 resisting force applied to the boulder, inducing a decrease in its velocity, i.e. a non-linear evolution
300 of its vertical displacement (Figure 10).

301 The temporal response trend of the energy dissipating devices is similar for all devices and for
302 the two impact tests (Figure 11). The force increases regularly till a threshold value is reached
303 (around 20 kN), which corresponds to the device activation. The force then oscillates around this
304 threshold value.

305 Similar evolution of the forces in the upstream cables is observed for the two impact tests (Figure
306 13). During the pre-tensile phase, a higher force is observed in cable P_{32} than in cable P_{31} . At the
307 beginning of the reaction phase, the force in P_{32} starts decreasing till $t = 120$ ms approximately,
308 before increasing again. In contrast, the force in P_{31} regularly increases until $t = 200$ ms. These
309 differences may be explained by the close relationships between the forces in the upstream cables
310 and the motion of the post extremity these cables are connected to. During the pre-tensile phase,
311 the progressive deformation of the net central panel induces a displacement of the extremity of
312 the two central posts towards the center of the barrier. It entails a larger force in P_{32} than in
313 P_{31} (Figure 13). At the beginning of the reaction phase, the activation of the energy dissipating
314 devices U5 and U7 increases the length of the supporting cables B_{UP} and C_{UP} , and the net stops
315 its motion toward the center of the barrier. It moves downward as the boulder continues moving
316 downward, which induces a motion of the posts both downward and towards their initial lateral
317 position. This motion first results in a decrease in the force in P_{32} and in an increase in P_{31} (Figure
318 11). When the initial lateral position of the posts is reached, the forces increase both in P_{31} and
319 P_{32} . Cable P_{42} experiences a more progressive loading and a lower maximum force than cables P_{31}
320 and P_{32} because it is located further from the impact zone.

321 Finally, in both tests, the forces in the energy dissipating devices L2 and L7 suggest asymmet-

322 rical lateral diffusion of the forces into the barrier (Figure 11). This is confirmed by the different
323 maximum elongations of the cables associated with these energy dissipating devices in figure 12
324 (SI_{Exp1} : 220 cm for the cable B_{LOW} (L2) and 247 cm for C_{LOW} (L7), SI_{Exp2} : 257 cm and 280
325 cm for the same quantities).

326 Despite the similar qualitative responses between the two tests, quantitative differences are
327 evidenced. First, for the first impact, SI_{Exp1} , the boulder is stopped earlier (Figure 10) and the
328 forces in the energy dissipating devices and in the upstream cables also vanish earlier (Figure 11
329 and 13). One can deduce that the impact duration is shorter in SI_{Exp1} than in SI_{Exp2} . In addition,
330 a shorter penetration is observed for SI_{Exp1} . Second, the response of the energy dissipating devices
331 is highly different from one test to the other and from one device to the other (Figure 11 and 12).
332 Significant differences in the maximum elongations of the cables are also observed, e.g. B_{LOW} :
333 220 cm for SI_{Exp1} and 257 cm for SI_{Exp2} . Finally, the time evolution of the forces in the upstream
334 cables are quantitatively different, and in particular that of cable P_{32} with different values and
335 times for the maximum forces peaks (24 kN and 26 kN at respectively 90 ms and 250 ms for
336 SI_{Exp1} , and 10 kN and 32 kN at respectively 75 ms and 215 ms for SI_{Exp2}). These results clearly
337 reveal the difference in response from one structure to the other.

338 These qualitative and quantitative analyses exhibit the structure response complexity, variabil-
339 ity and sensitivity for two similar structures subjected to an similar impact. The two tests provide
340 different responses and force distributions inside the structure. An asymmetrical behavior is also
341 observed for the force distribution and energy dissipating devices elongation. These observations
342 are attributed to little differences in the structure installation in terms of initial tension in cables
343 and exact geometry in particular, as well to the energy dissipating devices response variability.
344 Considering these differences highlighted between two similar impacts, we cannot expect one given
345 experimental result to be the representative response of the structure, but we can consider it as
346 one outcome.

347 3.2. Consecutive impacts test

348 The structure was subjected to 3 consecutive impacts experiments (CO_{Exp}^1 , CO_{Exp}^2 and CO_{Exp}^3)
349 at energies three times lower than for the single impact tests (90 kJ energy - corresponding to a 740
350 kg boulder at a velocity of 15.6 m/s). This test was performed without any repair nor maintenance

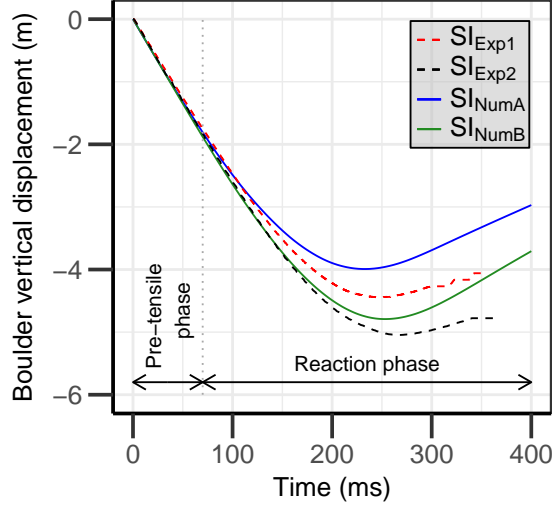


Figure 10: Boulder vertical displacement over time for single impact test: simulation results for models A and B, against the experimental data.

351 work. Due to recording issues, no real-time data were collected from the sensors during CO_{Exp}^2
 352 but the other measurements are available.

353 As for the single impact tests (section 3.1), pre-tensile and reaction phases are observed in
 354 the structure response. They are clearly identified for the first impact CO_{Exp}^1 with linear and
 355 non-linear parts on the curve giving the boulder vertical displacement over time but are almost
 356 absent for the third impact CO_{Exp}^3 (figure 14). Qualitative similarities between the single impact
 357 tests and the first impact CO_{Exp}^1 are also observed for the energy dissipating devices (Figure 15)
 358 and the upstream cables responses (Figure 16). During the first impact, the structure reorganizes
 359 in a geometrical configuration favoring the energy transfers from the impact zone to the anchors.

360 In the consecutive impacts, the initial configuration corresponds to the end of the previous
 361 impact after bloc removal and smaller geometrical changes are observed. As the duration of
 362 the pre-tensile phase is very limited for CO_{Exp}^3 , the boulder almost decelerates from the impact
 363 beginning. Hence, shorter impact duration and boulder maximum displacement are observed (3.56
 364 m and 1.20 m for respectively impacts 1 and 3) (Figure 14). In addition, the energy dissipating
 365 devices are activated earlier and their activation duration is about twice lower for CO_{Exp}^3 compared
 366 to CO_{Exp}^1 (figure 15). The forces in the upstream cables increase faster, from the impact beginning,
 367 and reach higher maximum values for the third impact (figure 16). This means that the top of the
 368 posts does not initially move towards the center of the barrier. These observations demonstrate

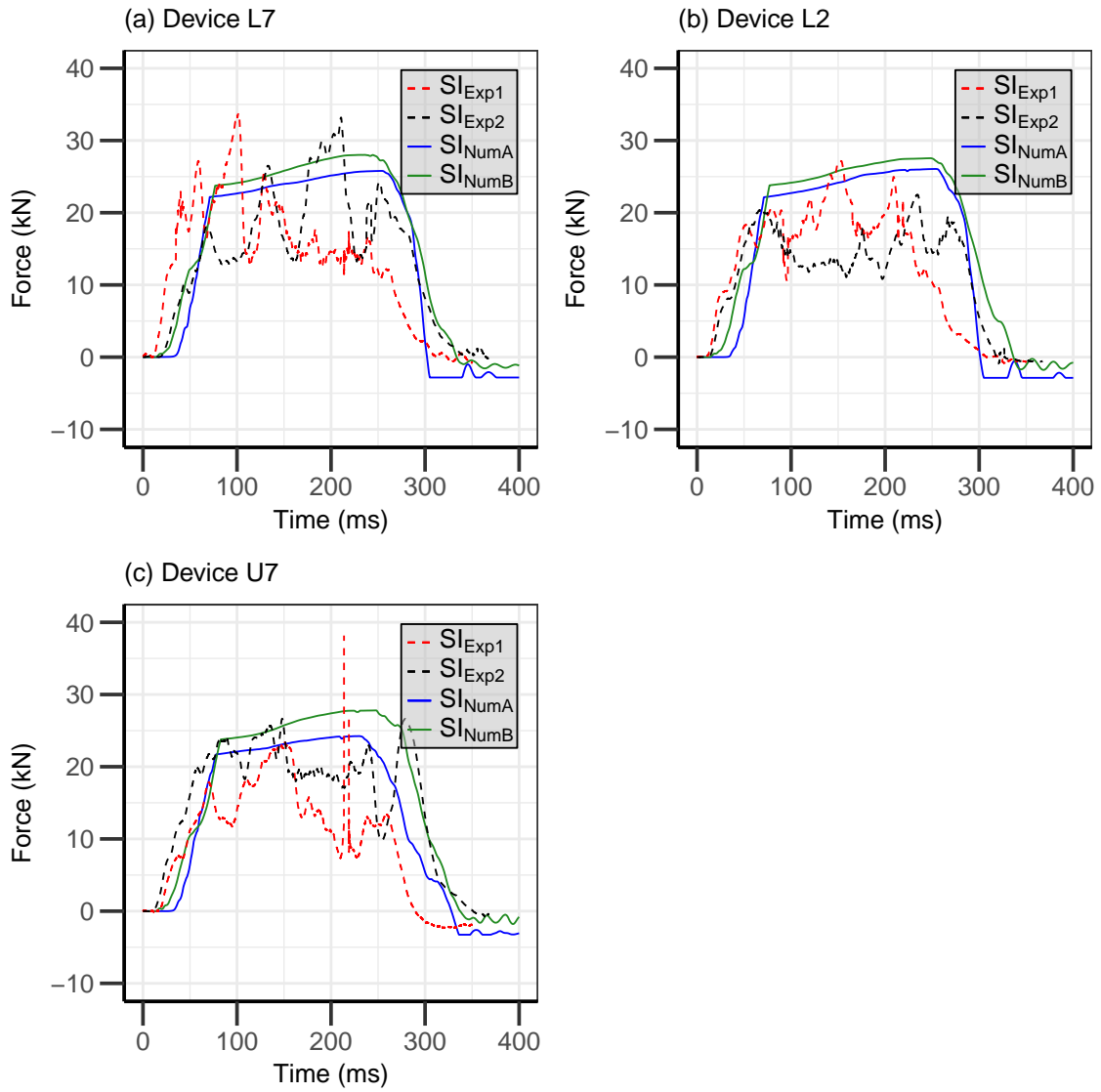


Figure 11: Evolution of the force acting within the energy dissipating devices, simulation results for models A and B against the experimental data: Device L7 (a), Device L2 (b), Device U7 (c).

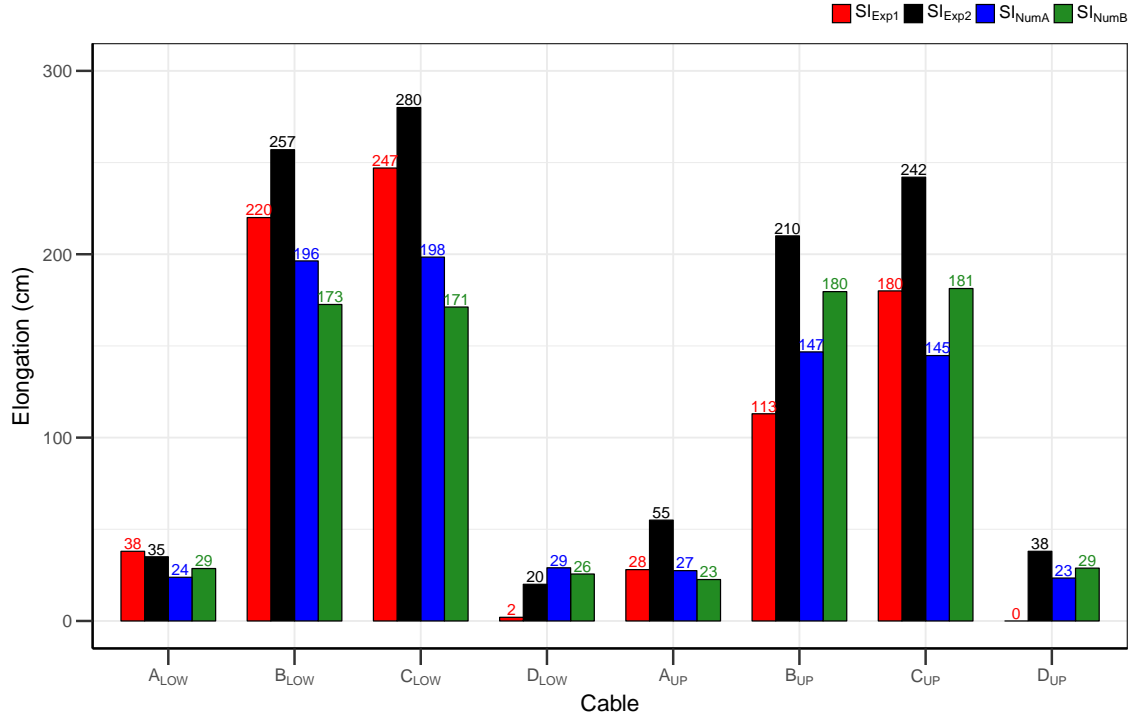


Figure 12: Cables elongation (sum of the elongations of the two energy dissipating devices connected to the cable) after impact for single impact tests, simulation results for models A and B against the experimental data.

369 an overall stiffer structure response for the third impact.

370 The post-impact elongation of the cables (table 5) evolves over the consecutive impact as well
 371 as it confirms the asymmetrical response of the structure. As for the evolution, results show that
 372 the cables elongation is higher during the first impact, when both considering the elongation of
 373 single cables and the sum of the elongations of all the cables. As for the asymmetrical response,
 374 higher elongations are observed for all three tests on upper cables A and B than in upper cables C
 375 and D, located on the other side of the structure with respect to the impact point. The opposite
 376 trend is observed focusing on the lower supporting cables, with higher values on cables C and D
 377 than in cables A and B. Comparison between upper and lower supporting cables also reveals that,
 378 in this latter case, elongations in the central part are lower (cables B and C) than in the former
 379 case.

380 The results from the first of the consecutive impact tests (CO_{Exp}^1) confirm the nature of the
 381 mechanical response of the structure to a single impact test. A different response is observed
 382 for the third impact (CO_{Exp}^3) with a very limited pre-tensile phase, leading to a stiffening of the
 383 structure. Similar as for the single impact tests, an asymmetrical response is observed in terms of

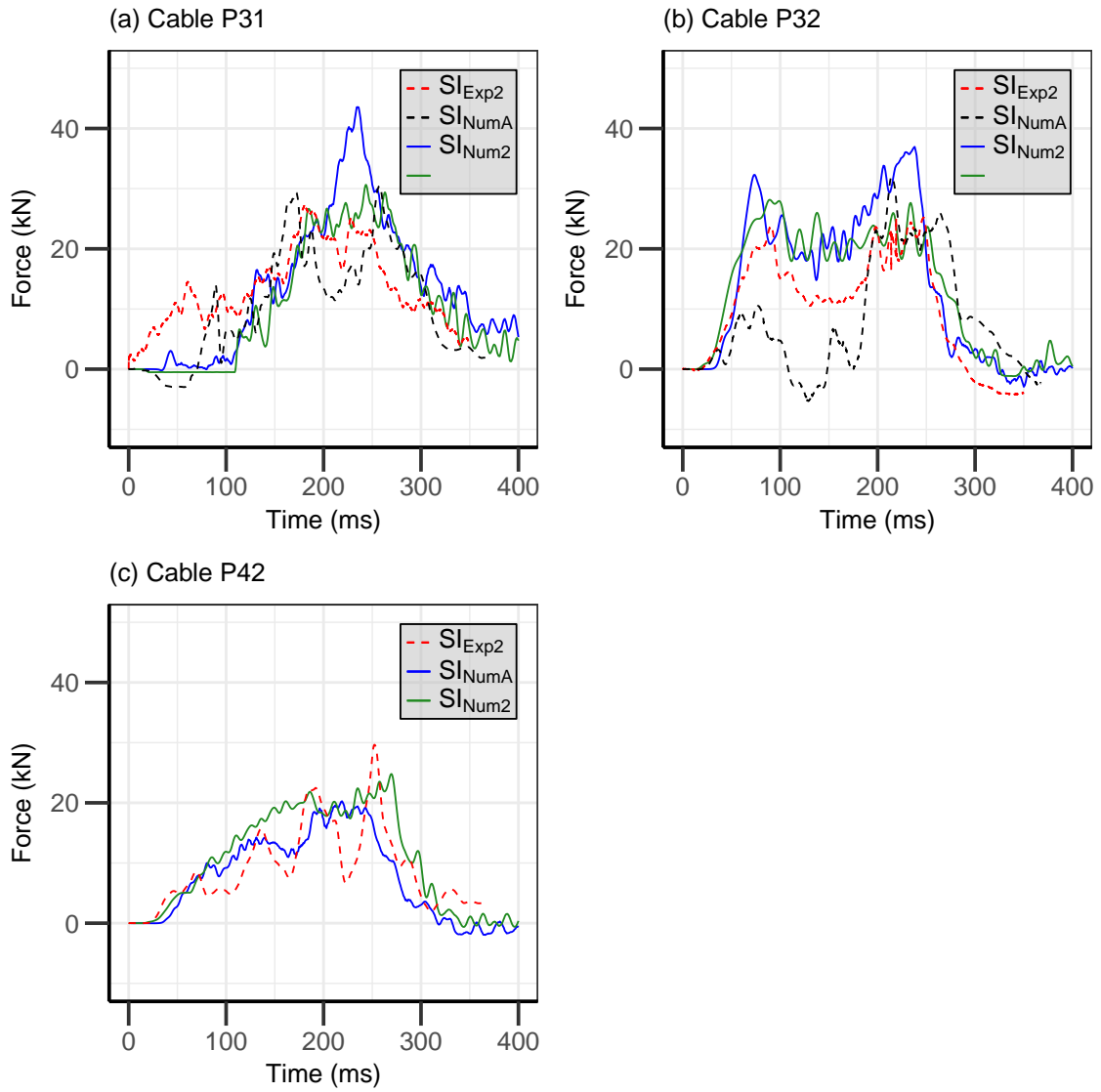


Figure 13: Evolution of the force acting into the upstream cables for single impact test, simulation results for models A and B against the experimental data: Cable P_{31} (a), Cable P_{32} (b), Cable P_{42} (c).

384 elongations of the energy dissipating devices and forces evolution in the structure components, for
 385 all impact tests.

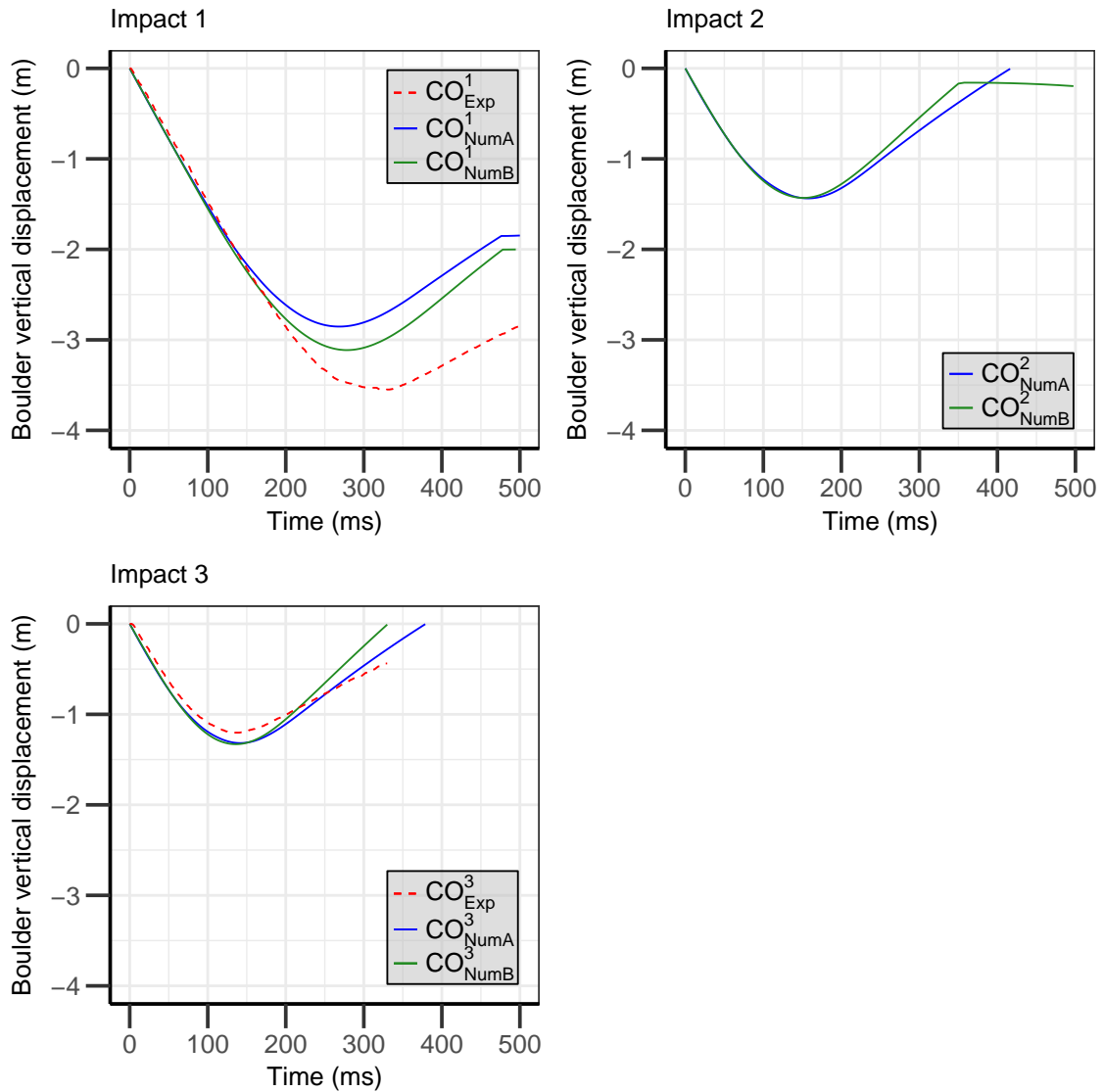


Figure 14: Evolution of the boulder vertical displacement of the net over time for the 3 consecutive impacts: simulation results from models A and B against experimental data.

386 4. Models predictive capacity

387 The experimental results (Section 3) show a complex two-phase response of the barrier. They
 388 also highlight the influence of the different components on the mechanical response. For example,
 389 the net rings subjected to either bending or tensile regimes [Nicot et al., 2001b, Escallón et al.,
 390 2014], the energy dissipating devices the response of which depends on the loading conditions
 391 [Castanon-Jano et al., 2017] and the connection between the cable and the net [Coulibaly et al.,
 392 2019] play major roles in the structure response. In this section, the numerical responses given by

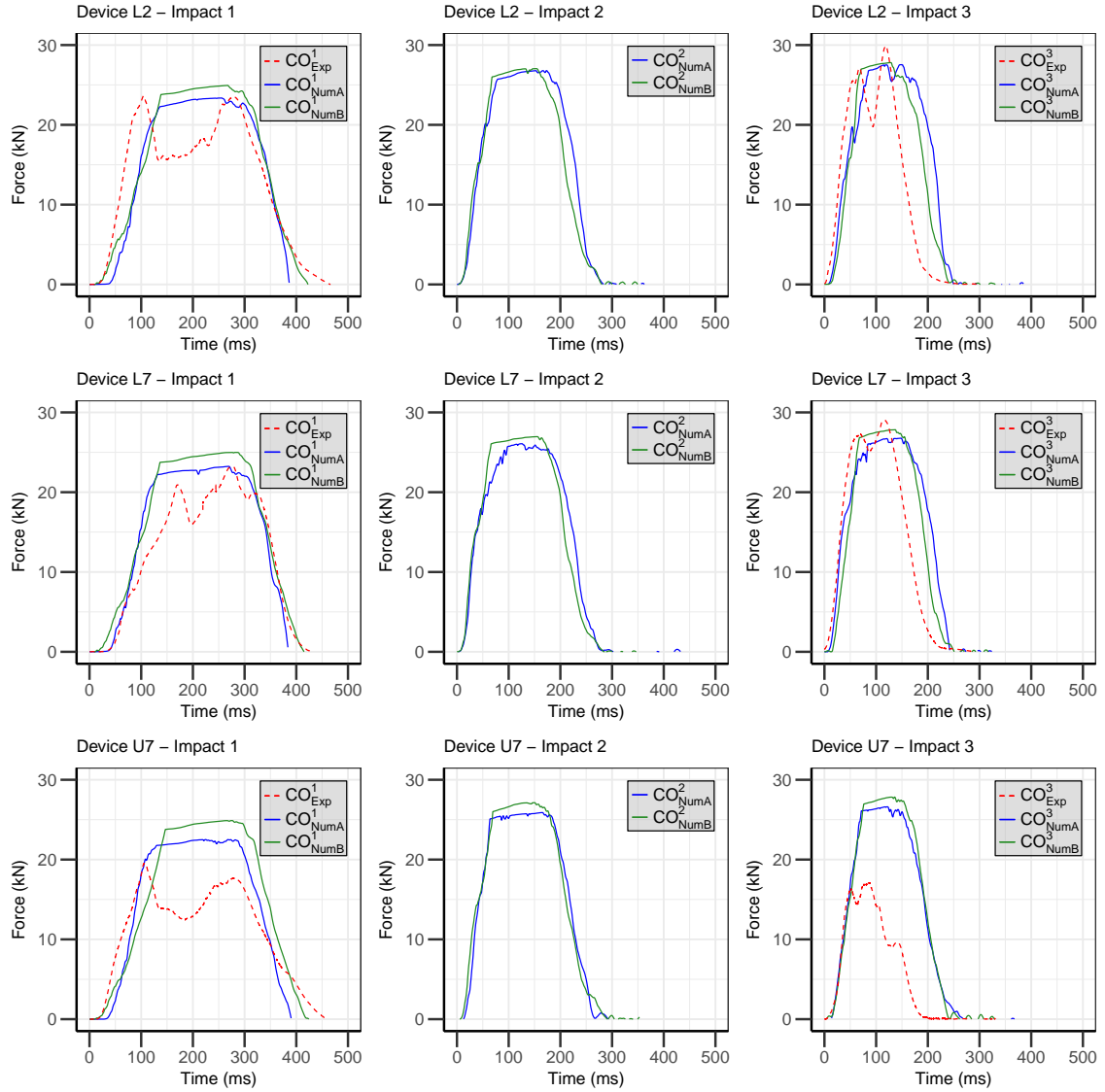


Figure 15: Energy dissipating devices L2, L7 and U7 force for the 3 consecutive impacts: simulation results from models A and B against experimental data.

	Upper supporting cables				Lower supporting cables			
	A_{UP}	B_{UP}	C_{UP}	D_{UP}	A_{LOW}	B_{LOW}	C_{LOW}	D_{LOW}
Impact 1	17	100	85	0	0	65	60	20
Impact 2	20	185	150	0	0	130	130	20
Impact 3	40	217	205	24	0	182	188	36

Table 5: Experimental cables elongation (sum of the elongations of the two energy dissipating devices connected to the cable) for consecutive impacts. All data are in cm.

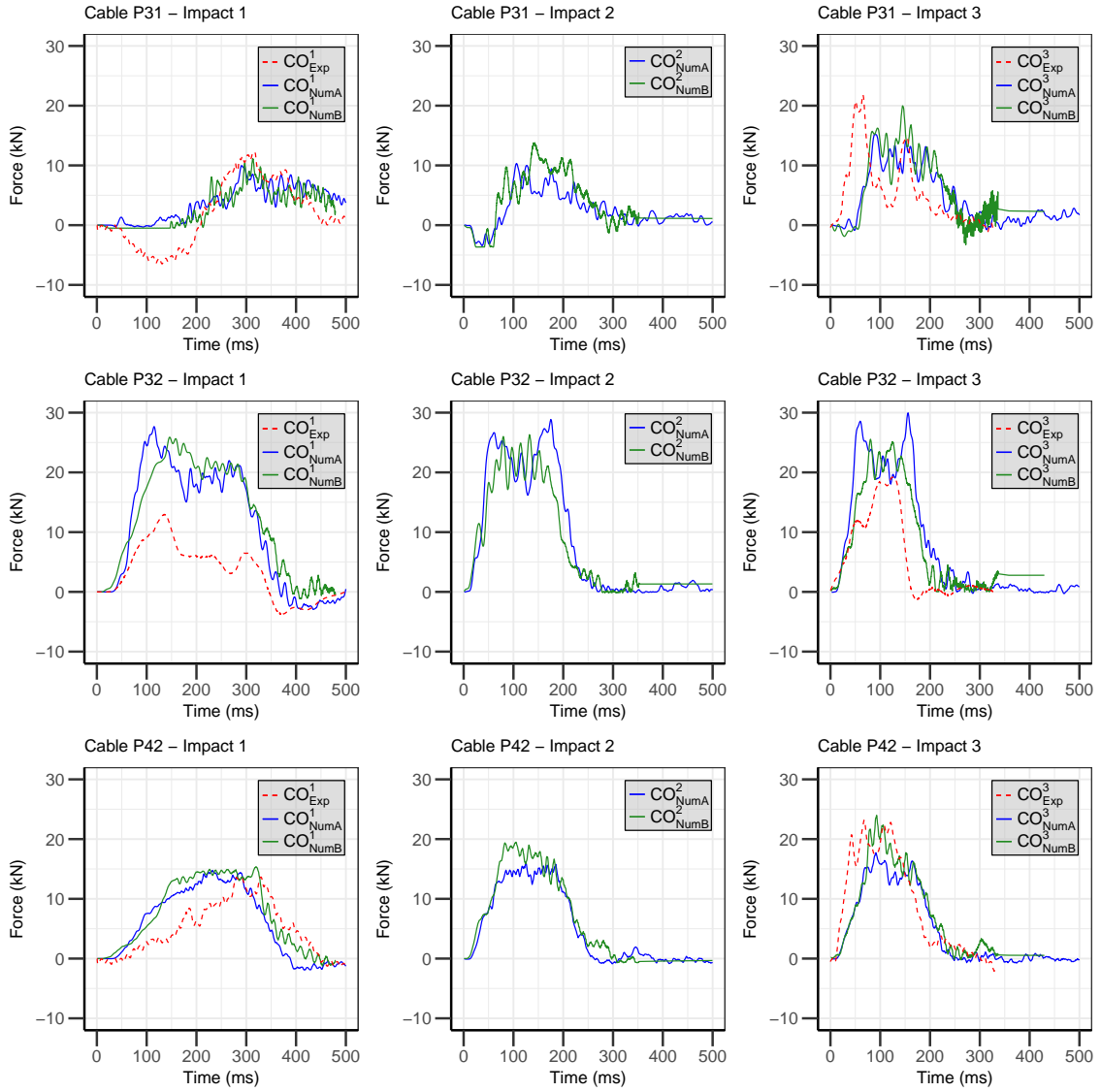


Figure 16: Upstream cables P_{31} , P_{32} and P_{42} force for the 3 consecutive impacts: simulation results from models A and B against experimental data.

393 the two models for both single and consecutive impacts conditions are analyzed. These predictions
394 are obtained without back analysis on the experimental results. The models predictive capacity
395 is qualitatively and quantitatively explored studying the responses of the global structure, of the
396 energy dissipating devices and of the upstream cables.

397 4.1. Single impact test

398 During the single high velocity impact, the structural elements are loaded up to the plasticity
399 limit which needs to be reproduced with the models. Single impact tests were simulated with
400 models A and B, respectively labelled as SI_{NumA} and SI_{NumB} .

401 The two models qualitatively reproduce the experimental global response of the barrier, the
402 forces into the energy dissipating devices and into the upstream cables. In particular, both models
403 reproduce the pre-tensile and reaction phases observed experimentally (Section 3.1) with the linear
404 and non-linear parts of the boulder vertical displacement curve (Figure 10).

405 As for the dissipating devices, differences appear between experiments and simulations. In
406 accordance with the dissipating device model implemented, the numerical response shows a sharp
407 increase in the force up to the threshold value, followed by a slightly increasing plateau until
408 the end of the impact. By contrast, experiments reveal significantly different responses in terms
409 of activation force level and post-activation force evolution (Figure 11). The energy dissipating
410 devices experimentally show slightly lower activation values and mean forces during activation. The
411 activation duration is similar (Figure 11) and higher elongations of the energy dissipating devices
412 are observed experimentally (Figure 12). These differences are attributed to the model calibration,
413 based on quasi-static test results. Such a loading has been shown to result in a different response
414 compared to dynamic loading [Castanon-Jano et al., 2017]. Second, the variability in activation
415 force is inherent to the dissipating devices technology. This variability should be considered in the
416 numerical simulations.

417 Despite the differences in the energy dissipating devices responses, the evolution of the forces
418 for the upstream cables closest (P_{31} and P_{32}) and farthest (P_{42}) from the impact zone are rather
419 well predicted (Figure 13). This demonstrates the models ability in predicting the propagation of
420 the forces inside the structure from the impact zone to the anchors, even at a long distance from
421 the impact zone (cable P_{42}).

422

423 In addition to the satisfying qualitative results, the simulations quantitatively compare well to
 424 the experimental, with variable accuracy for both models regarding the studied quantities.

425 The maximum boulder vertical displacement predicted by the simulations (Figure 10) is ac-
 426 ceptable when considering the variability of the experimental results (Table 6) (maximum error of
 427 21% : SI_{NumA} vs. SI_{Exp1}). Both models also show acceptable prediction for the maximum forces
 428 in the cables (Figure 13).

429 A lateral symmetry is observed numerically for the force in devices L2 and L7 and for the
 430 elongations of cables B and C (Figures 11 and 12) while the experimental evolutions of these
 431 quantities exhibit significant asymmetry. Both models also tend to underestimate the lower cables
 432 elongation; this is more pronounced for model B (Figure 12). Finally, model A shows slightly higher
 433 maximum forces for cables P_{31} and P_{32} and lower ones for cable P_{42} compared to the experiments,
 434 while the forces predicted by model B forces are in good agreement with the experiments (Figure
 435 13).

436 Even though the maximum forces, boulder displacement and elongations of the energy dissi-
 437 pating devices show deviation from the experimental values, the overall trends of the evolution of
 438 the forces inside the structure are quite well predicted. This proves that the modeling assump-
 439 tions made for the main elements of the structure (net, energy dissipating devices, connection
 440 between supporting cables and net) are also robust when high intensity loading conditions hold.
 441 Considering the global structure, the diffusion of the forces from the impact zone to the anchors
 442 is respected. These results validate the global modeling method used for both models in single
 443 impact conditions.

	SI_{Exp1}	SI_{Exp2}	SI_{NumA}	SI_{NumB}
Maximum boulder displacement (m)	-4.44	-5.05	-4.00	-4.79

Table 6: Maximum boulder vertical displacement for single impact tests, experimental and numerical results.

444 4.2. Consecutive impacts test

445 In consecutive impact conditions, the structure is impacted three times with a lower boulder
 446 velocity. The complexity of this loading condition stems from the impact repetition which implies
 447 unloading and reloading of the elements of the structure. The two models were tested with con-

	$Displ_{Max} (m)$			$t_{stop} (ms)$		
	Exp	model A	model B	Exp	model A	model B
CO^1	3.56	2.85	3.11	325	269	278
CO^2	-	1.44	1.43	166	158	152
CO^3	1.20	1.32	1.33	130	141	136

Table 7: Maximum boulder vertical displacement ($Displ_{Max}$) and time to stop the boulder (t_{stop}), experimental and numerical results for each impact.

448 secutive impacts: CO^1_{NumA} , CO^2_{NumA} and CO^3_{NumA} for model A, and CO^1_{NumB} , CO^2_{NumB} and
449 CO^3_{NumB} for model B.

450 The first impact numerical response is qualitatively similar to the single impact one, as observed
451 experimentally in section 3.2. The good prediction of the first impact was expected regarding the
452 good accuracy of the single impact models predictions (Section 4.1). Regarding the subsequent
453 impacts, the stiffening of the structure is predicted by both models with the reduction of the pre-
454 tensile phase duration (Figure 14), the impact duration decreasing (Figure 15) and the maximum
455 forces increasing (Figure 16). The trends for the first and third impacts, as well as the increasing
456 loading rate are predicted for both the energy dissipating devices (Figure 15) and upstream cables
457 evolution of the forces (Figure 16).

458 Quantitatively, both models show lower maximum boulder displacement for the first impact
459 compared to the experimental results, but a good accuracy is observed for the third impact (Figure
460 14 and Table 7). The large difference in impact duration between the first and second impact
461 observed numerically confirms that the geometrical reorganization occurs mainly during the first
462 impact. As observed for the single impact test, lower elongation of the energy dissipating devices is
463 obtained due to their modeling assumption and quasi-static calibration (Figure 17). Even though
464 a delay in the loading of the upstream cables is observed, the force in the anchors are predicted
465 from the closest to the farthest of the impact zone (Table 8 and Figure 16).

466 Overall, the models reproduce the diffusion of the forces into the structure with an accurate
467 timing for each impact. The accuracy increases with the impacts showing that, once the structure
468 geometry after the first impact is predicted, the response of the following impacts is easier to
469 reproduce. However, the prediction of these following impacts implies a good accuracy in the
470 loading and unloading responses of the different structural elements modeling. Moreover, despite
471 differences in the modeling assumptions, the two models show close trends and maximum values
472 in the respective responses.

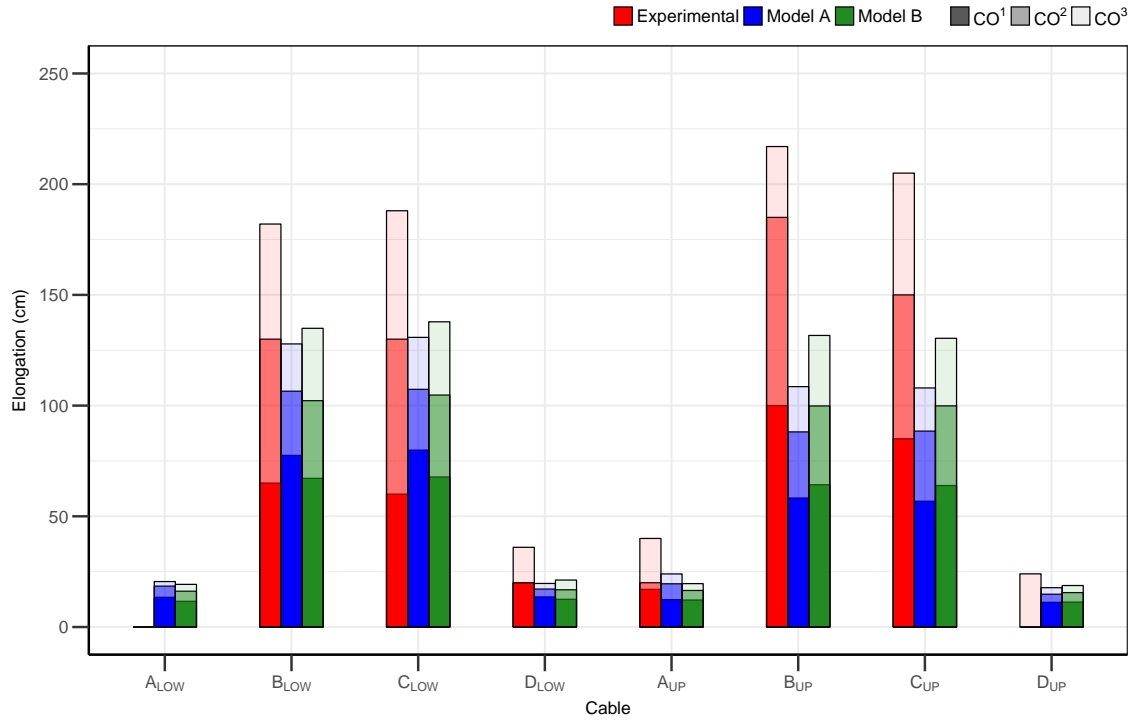


Figure 17: Cables elongation (sum of the elongations of the two energy dissipating devices connected to the cable) for the 3 consecutive impacts: simulation results from models A and B against experimental data.

	Maximum force P_{31} (kN)			Maximum force P_{32} (kN)			Maximum force P_{42} (kN)		
	Exp	model A	model B	Exp	model A	model B	Exp	model A	model B
CO^1	12	10	12	13	28	26	13	16	15
CO^2	-	11	15	-	30	27	-	17	20
CO^3	22	15	20	19	31	26	23	18	25

Table 8: Maximum forces in the upstream cables P_{31} , P_{32} , and P_{42} for each impact: experimental and numerical results.

473 5. Conclusion

474 In this paper, the capacities and limitations of DEM modelling approaches for the assessment
475 of the response of rockfall protection barrier were investigated. For that purpose, the response of
476 a 270 kJ in capacity flexible barrier was studied using a subsequent experimental campaign and
477 two discrete element method models.

478 Experimentally, single impact tests emphasized, despite a significant variability in the structure
479 response, a behavior that consists of a pre-tensile phase followed by a reaction one. For consecutive
480 impacts, the importance of the pre-tensile phase reduces along the impacts, as a consequence of a
481 global stiffening of the structure.

482 The two models are developed using different codes but the same modeling approach. It consists
483 in modeling and calibrating separately each element of the barrier, and assembling them together to
484 get the full structure model. The models are finally validated in comparison with the experimental
485 full scale tests results without back analysis (single and consecutive impacts). The complexity of
486 both the structure and the impact conditions leads to critical validation conditions for the models,
487 multiple aspects of their responses being explored in details.

488 The two models exhibit similarities in the modelling of the energy dissipating devices, the
489 posts, the anchors and the boulder. On the contrary, two different approaches with different level
490 of complexity are chosen for modeling the net and cable-net connection, in particular. Despite
491 these differences on these two main structure components, both models allow accurate prediction
492 of the experimental data for single and consecutive impacts, in particular from a qualitative point
493 of view. For single impacts, the pre-tensile and reaction phases are correctly reproduced and the
494 two models are able to predict the large deformations of the structure and the plastic strains
495 occurring. For consecutive impact conditions, the models allow accurate prediction from the first
496 to the third impact which shows that they are able to reproduce fairly the loading and unloading
497 responses of the structure.

498 Although the comparison between the two models is not the purpose of this study, it is in-
499 teresting to note that, even if both models reveal ability to predict the response of the structure,
500 some characteristics are sometimes better predicted by one of the two models. For example, model
501 B shows a better accuracy for the boulder vertical displacement (Figure 10) while model A shows

502 a better prediction for the distribution of the energy dissipating devices elongation (Figure 12).
503 This shows that the validation of a numerical model as well as the comparison between different
504 models should not be only limited to one output, but should also consider the structure global
505 response. Indeed, a model can be accurate for some outputs but provide bad predictions for other
506 ones, depending on its initial purpose and level of complexity.

507 The good predictive capacities of the models show that discrete element method is a well
508 adapted numerical approach for the modeling of flexible rockfall barriers. Indeed, it makes it
509 possible to implement complex behavior laws, including unloading phases, thanks to the explicit
510 Lagrangian formulation of the method. These good predictive capacities also prove the relevance
511 of the calibration procedure based on quasi-static calibration of the different structural elements
512 models, such as the energy dissipating devices or the net.

513 Finally, considering the acceptable computation time and results, a practical use of these models
514 and of the associated calibration procedures can be considered as a friendly helping tool for the
515 design of new structures, in particular for a preliminary design of new prototypes. However, using
516 these models to get an exact deterministic response of the structure does not seem relevant, because
517 small differences between the real structure and that modeled may have a significant influence on
518 the structure response. For example, the observed asymmetry results from this type of difference
519 and it is not modelled. Finally, these models can be used for more thorough exploration such as
520 parametric analysis, or as training data for meta-models [Toe et al., 2018, Coulibaly et al., 2019].

521 **Acknowledgement**

522 This research was conducted within the frame of the French National project C2ROP. the
523 authors would like to thank all the partners and in particular companies such as CAN and NGE
524 Fondations.

525 **References**

526 A. Albaba, S. Lambert, F. Kneib, B. Chareyre, and F. Nicot. Dem modeling of a flexible barrier
527 impacted by a dry granular flow. *Rock Mechanics and Rock Engineering*, 50(11):3029–3048, Nov
528 2017. ISSN 1434-453X. doi: 10.1007/s00603-017-1286-z. URL [https://doi.org/10.1007/
529 s00603-017-1286-z](https://doi.org/10.1007/s00603-017-1286-z).

530 R. D. Andrew, D. A. Fry, and R. E. Bookwalter. *Field Testing and Evaluation of Various Rock*
531 *Fall Control System*. Chama ValleyProductions, LLC, Chama Valley, NM (USA), 1998.

532 D. Bertrand, F. Nicot, P. Gotteland, and S. Lambert. Discrete element method (dem) numerical
533 modeling of double-twisted hexagonal mesh. *Canadian Geotechnical Journal*, 45(8):1104–1117,
534 2008. doi: 10.1139/T08-036. URL <https://doi.org/10.1139/T08-036>.

535 D. Bertrand, A. Trad, A. Limam, and C. Silvani. Full-scale dynamic analysis of an innovative
536 rockfall fence under impact using the discrete element method: from the local scale to the
537 structure scale. *Rock Mechanics and Rock Engineering*, 45:885–900, Sept. 2012. doi: 10.1007/
538 s00603-012-0222-5.

539 F. Bourrier, S. Lambert, and J. Baroth. A reliability-based approach for the design of rockfall
540 protection fences. *Rock Mechanics and Rock Engineering*, 48(1):247–259, Jan 2015. ISSN 1434-
541 453X. doi: 10.1007/s00603-013-0540-2. URL <https://doi.org/10.1007/s00603-013-0540-2>.

542 L. Castanon-Jano, E. Blanco-Fernandez, D. Castro-Fresno, and F. Ballester-Muñoz. Energy dissi-
543 pating devices in falling rock protection barriers. *Rock Mechanics and Rock Engineering*, 50(3):
544 603 – 619, 2017.

545 L. Castanon-Jano, E. Blanco-Fernandez, D. Castro-Fresno, and D. Ferreño. Use of explicit fem
546 models for the structural and parametrical analysis of rockfall protection barriers. *Engineering*
547 *Structures*, 166:212 – 226, 2018. ISSN 0141-0296. doi: [https://doi.org/10.1016/j.engstruct.2018.](https://doi.org/10.1016/j.engstruct.2018.03.064)
548 03.064. URL <http://www.sciencedirect.com/science/article/pii/S0141029617318461>.

549 A. Cazzani, L. Mongiovì, and T. Frenez. Dynamic finite element analysis of interceptive devices for
550 falling rocks. *International Journal of Rock Mechanics and Mining Sciences*, 39:303–321, 2002.

551 J. Coulibaly. *Modélisation numérique discrète du comportement mécanique sous impact des struc-*
552 *tures d’écrans de filets pare-pierres*. PhD thesis, University Grenoble-Alpes, Grenoble (France),
553 2017a. (in French).

554 J. Coulibaly, M.-A. Chanut, S. Lambert, and F. Nicot. Toward a generic computational approach
555 for flexible rockfall barrier modeling. *Rock Mechanics and Rock Engineering*, 05 2019. doi:
556 10.1007/s00603-019-01878-6.

557 J. B. Coulibaly, M.-A. Chanut, S. Lambert, and F. Nicot. Non-linear discrete mechanical model
558 of steel rings. *Journal of Engineering Mechanics*, 143(9):04017087, 2017b. doi: 10.1061/(ASCE)
559 EM.1943-7889.0001303. URL [https://ascelibrary.org/doi/abs/10.1061/%28ASCE%29EM.
560 1943-7889.0001303](https://ascelibrary.org/doi/abs/10.1061/%28ASCE%29EM.1943-7889.0001303).

561 J. B. Coulibaly, M.-A. Chanut, S. Lambert, and F. Nicot. Sliding cable modeling: an attempt at
562 a unified formulation. *International Journal of Solids and Structures*, 130-131:1–10, 01 2018.

563 EOTA. *Falling Rock Protection Kits. EAD 340059-00-0106, 2018/C 417/07*. European Organiza-
564 tion for Technical Approvals, 2018.

565 J. Escallón, C. Wendeler, E. Chatzi, and P. Bartelt. Parameter identification of rockfall pro-
566 tection barrier components through an inverse formulation. *Engineering Structures*, 77:1
567 – 16, 2014. ISSN 0141-0296. doi: <https://doi.org/10.1016/j.engstruct.2014.07.019>. URL
568 <http://www.sciencedirect.com/science/article/pii/S0141029614004374>.

569 J. Escallón, v. Boetticher, C. Wendeler, E. Chatzi, and P. Bartelt. Mechanics of chain-link
570 wire nets with loose connections. *Engineering Structures*, 101:68 – 87, 2015. ISSN 0141-0296.
571 doi: <https://doi.org/10.1016/j.engstruct.2015.07.005>. URL [http://www.sciencedirect.com/
572 science/article/pii/S0141029615004393](http://www.sciencedirect.com/science/article/pii/S0141029615004393).

573 K. Feyrer, editor. *Wire Ropes*. Springer, 2015.

574 W. Gerber and A. Böll. Type-testing of rockfall barriers - comparative results. In *International
575 Symposium Interpraevent*, pages 189–198, Munich (Germany), April 2006.

576 G. Gottardi and L. Govoni. Full-scale modelling of falling rock protection barriers. *Rock Me-
577 chanics and Rock Engineering*, 43(3):261–274, May 2010. ISSN 1434-453X. doi: 10.1007/
578 s00603-009-0046-0. URL <https://doi.org/10.1007/s00603-009-0046-0>.

579 J. P. Hambleton, O. Buzzi, A. Giacomini, M. Spadari, and S. W. Sloan. Perforation of flexible
580 rockfall barriers by normal block impact. *Rock Mechanics and Rock Engineering*, 46(3):515–526,
581 2013.

582 C. Heiss. Characteristics of the testing of rock fall protection kits on transversal test sites on

583 example "Steirischer Erzberg". In *International Symposium Interpraevent*, pages 49–58, Riva
584 del Garda (Italy), May 2004.

585 S. Lambert and F. Nicot, editors. *Rockfall Engineering*. Wiley, 2011.

586 M. T. McCauley, B. W. Works, and S. A. Naramore. *Rockfall Mitigation*. California Department
587 of Transportation, Sacramento, California (USA), 1985.

588 A. Mentani, A. Giacomini, O. Buzzi, L. Govoni, G. Gottardi, and S. Fityus. Numerical modelling
589 of a low-energy rockfall barrier: New insight into the bullet effect. *Rock Mechanics and Rock
590 Engineering*, 49(4):1247–1262, Apr 2016. ISSN 1434-453X. doi: 10.1007/s00603-015-0803-1.
591 URL <https://doi.org/10.1007/s00603-015-0803-1>.

592 A. Mentani, L. Govoni, A. Giacomini, G. Gottardi, and O. Buzzi. An equivalent continuum
593 approach to efficiently model the response of steel wire meshes to rockfall impacts. *Rock Me-
594 chanics and Rock Engineering*, Apr 2018. ISSN 1434-453X. doi: 10.1007/s00603-018-1490-5.
595 URL <https://doi.org/10.1007/s00603-018-1490-5>.

596 H. Muraishi, M. Samizo, and T. Sugiyama. Development of a flexible low-energy rockfall protection
597 fence. *Quarterly Report of Railway Technical Research Institute*, 46(3):161–166, 2005.

598 F. Nicot, B. Cambou, and G. Mazzoleni. Design of rockfall restraining nets from a dis-
599 crete element modelling. *Rock Mechanics and Rock Engineering*, 34(2):99–118, 2001a. doi:
600 10.1007/s006030170017. URL <https://doi.org/10.1007/s006030170017>.

601 F. Nicot, B. Cambou, and G. Mazzoleni. From a constitutive modelling of metallic rings to the
602 design of rockfall restraining nets. *International Journal for Numerical and Analytical Methods
603 in Geomechanics*, 25(1):49–70, 2001b.

604 D. Peila, S. Pelizza, and F. Sassudelli. Evaluation of behaviour of rockfall restraining nets by full
605 scale tests. *Rock Mechanics and Rock Engineering*, 31(1):1–24, Feb 1998. ISSN 1434-453X. doi:
606 10.1007/s006030050006. URL <https://doi.org/10.1007/s006030050006>.

607 D. Smith and J. Duffy. Field test and evaluation of rockfall restraining nets. *California Department
608 of Transportation*, 1990.

- 609 M. Spadari, A. Giacomini, O. Buzzi, and J. P. Hambleton. Prediction of the bullet effect for rockfall
610 barriers: a scaling approach. *Rock Mechanics and Rock Engineering*, 45(2):131–144, 2012.
- 611 K. Thoeni, C. Lambert, A. Giacomini, and S. W. Sloan. Discrete modelling of hexagonal wire
612 meshes with a stochastically distorted contact model. *Computers and Geotechnics*, 49(Complete):
613 158–169, 2013. doi: 10.1016/j.compgeo.2012.10.014.
- 614 D. Toe, A. Mentani, L. Govoni, F. Bourrier, G. Gottardi, and S. Lambert. Introducing meta-
615 models for a more efficient hazard mitigation strategy with rockfall protection barriers. *Rock*
616 *Mechanics and Rock Engineering*, 51(4):1097–1109, Apr 2018. ISSN 1434-453X. doi: 10.1007/
617 s00603-017-1394-9. URL <https://doi.org/10.1007/s00603-017-1394-9>.
- 618 P. V. Tran, K. Maegawa, and S. Fukada. Experiments and dynamic finite element analysis of
619 a wire-rope rockfall protective fence. *Rock Mechanics and Rock Engineering*, 46(5):1183–1198,
620 2013. ISSN 1434-453X. doi: 10.1007/s00603-012-0340-0. URL [https://doi.org/10.1007/
621 s00603-012-0340-0](https://doi.org/10.1007/s00603-012-0340-0).
- 622 A. Volkwein. Numerical simulation of flexible rockfall protection systems. In *International Con-*
623 *ference on Computing in Civil Engineering*, page 11. ASCE, 2005. doi: 10.1061/40794(179)122.
624 URL <https://ascelibrary.org/doi/abs/10.1061/40794%28179%29122>.
- 625 A. Volkwein, K. Schellenberg, V. Labiouse, F. Agliardi, F. Berger, F. Bourrier, L. K. A. Dor-
626 ren, W. Gerber, and M. Jaboyedoff. Rockfall characterisation and structural protection – a
627 review. *Natural Hazards and Earth System Sciences*, 11(9):2617–2651, 2011. doi: 10.5194/
628 nhess-11-2617-2011. URL <https://www.nat-hazards-earth-syst-sci.net/11/2617/2011/>.
- 629 V. Šmilauer et al. Using and programming. In *Yade Documentation 2nd ed.* The Yade Project,
630 2015. doi: 10.5281/zenodo.34043. <http://yade-dem.org/doc/>.
- 631 Z. Yu, Y. Qiao, L. Zhao, H. Xu, S. Zhao, and Y. Liu. A simple analytical method for evalu-
632 ation of flexible barrier part 1 : Working mechanism and analytical solution. *Advanced Steel*
633 *Construction*, 14(2):115–141, 04 2018. doi: 10.18057/IJASC.2018.14.2.1.